International Journal of Nanomedicine

Dovepress
Taylor & Francis Group

Open Access Full Text Article

ORIGINAL RESEARCH

Carbon Dots Derived from *Ligusticum chuanxiong* Alleviate Acute Kidney Injury by Scavenging ROS and Restoring Mitochondrial Homeostasis

Sen Liu[1,*], Siyao Sun[1,2,*], Hang Li[3], Hongli Zhou[1], Xiangfei Cui[1], Shiyan Ruan[1], Yong Liu[1], Yao Tong[4], Miaomiao Lu[1]

[1]Department of Nephrology, the First Affiliated Hospital of Jinzhou Medical University, Jinzhou, 121000, People's Republic of China; [2]Department of Critical Care Medicine, Huludao Central Hospital, Huludao, 125000, People's Republic of China; [3]Department of Radiation Oncology, The First Affiliated Hospital of Jinzhou Medical University, Jinzhou, 121000, People's Republic of China; [4]Department of Cardiovascular Medicine, Chinese PLA Unit 92493 Hospital, Huludao, 125000, People's Republic of China

*These authors contributed equally to this work

Correspondence: Miaomiao Lu, Email miaomiaolu2012@163.com

Purpose: Acute kidney injury (AKI) is a severe clinical condition with high morbidity and mortality that lacks effective therapies. Carbon dots (CDs) derived from traditional Chinese medicine ingredients have emerged as promising therapeutic agents because of their favorable biosafety profile and potent antioxidant and anti-inflammatory properties. In this study, the therapeutic effects of CDs derived from *Ligusticum chuanxiong* (LC-CDs) were investigated in an ischemia-reperfusion injury AKI model, and their underlying molecular mechanisms were elucidated.

Methods: LC-CDs were developed through a facile hydrothermal method and were used to treat an ischemia-reperfusion AKI rat model and HK-2 cells with hypoxia/reoxygenation injury.

Results: LC-CDs with uniform nanostructures, graphitic carbon structures, and multiple chemical functional groups on the surface were successfully synthesized. The LC-CDs exhibited excellent hydrophilicity, chemical reactivity, and unique optical properties. Treatment with the LC-CDs significantly reduced creatinine and blood urea nitrogen levels and alleviated pathological damage in renal tissue. Additionally, the LC-CDs effectively cleared reactive oxygen species, reduced oxidative stress levels, and mitigated mitochondrial damage. Treatment with the LC-CDs also decreased renal tissue expression of key inflammatory factors (IL-1β, IL-6, and TNF-α). Transcriptome analysis revealed that differentially expressed genes associated with the LC-CDs were primarily involved in the autophagy, and inflammatory signaling pathways. Further subcellular fractionation and fluorescence localization analyses confirmed that the LC-CDs accumulated in and targeted mitochondria, suggesting that mitochondria are the primary organelle target through which the LC-CDs exert their effects. Autophagy-related signaling pathways likely also played a critical role in mediating the therapeutic efficacy of the LC-CDs.

Conclusion: The LC-CDs demonstrated considerable therapeutic potential in an AKI model through their antioxidant, anti-inflammatory, and autophagy regulation. Their outstanding biocompatibility, multifunctional synergistic properties, and well-defined molecular targets provide a crucial foundation for the development of novel nanomedicines and kidney-targeted delivery systems.

Keywords: carbon quantum dots, *Ligusticum chuanxiong*, acute kidney injury, oxidative stress, mitochondrial homeostasis

Introduction

Acute kidney injury (AKI) is a clinical syndrome characterized by a rapid decline in renal function, and it is associated with high incidence and mortality rates.[1] The pathological drivers of AKI include excessive oxidative stress, dysregulated inflammatory responses, and organelle dysfunction, particularly within the mitochondria.[2] Renal ischemia-reperfusion (I/R) injury is a major cause of AKI that disrupts cellular homeostasis,[3] particularly in the mitochondria-dense proximal tubules. The overproduction of reactive oxygen species (ROS) damages cellular structures and causes mitochondrial permeability transition pores to open, thereby exacerbating renal tubular cell injury and contributing to the loss of renal function.[4] Current

https://doi.org/10.2147/IJN.S577611
Received: 29 October 2025
Accepted: 31 March 2026
Published: 8 April 2026

clinical interventions for AKI are generally limited to supportive care and renal replacement therapies.[5] No effective pharmacological interventions have been developed that target the pathological mechanisms underlying AKI.

Ligusticum chuanxiong has a long history of use in traditional Chinese medicine to treat kidney disorders, with its efficacy in this context supported by a robust empirical foundation.[6] Its active compound, ligustrazine, can reduce the extent of AKI by promoting microcirculation, mitigating inflammation, and eliminating ROS.[7,8] However, several pharmacokinetic drawbacks limit the clinical application of *L. chuanxiong* and ligustrazine, including poor water solubility, low oral bioavailability, rapid metabolic degradation, and considerable interindividual variability in treatment effectiveness.[9,10] These problems result in *L. chuanxiong* having inconsistent therapeutic efficacy and increase the difficulty of targeted renal delivery, considerably limiting the clinical potential of this traditional remedy.[11]

The development of nanotechnology has created new opportunities for therapeutic intervention.[12] Carbon-based nanomaterials, particularly carbon quantum dots (CDs), have emerged as a promising platform for drug delivery and bioactivity enhancement.[13,14] CDs have modifiable surface properties and unique physicochemical attributes at the nanoscale,[15] and their small size (typically <10 nm) enables passive renal targeting through glomerular filtration, facilitating accumulation in injury-prone tubular regions.[16] This intrinsic renal tropism addresses the delivery challenges associated with traditional herbal extracts.

In consideration of these features, we hypothesized that CDs derived from *L. chuanxiong* (LC-CDs) can serve as an integrated nanoplatform that achieves therapeutic activity through targeted delivery (Figure 1). In addition to a favorable pharmacokinetic profile, CDs have notable enzyme-mimetic capabilities,[17] which are largely attributable to their oxygen-rich surface functional groups and expansive conjugated planes.[18] These properties endow CDs with potent ROS-scavenging capacity, positioning them as ideal agents to combat AKI-related oxidative stress.[19,20] Furthermore, CDs demonstrate considerable water solubility and colloidal stability because of their diversity of surface functional groups, with this facilitating bioavailability and enabling consistent therapeutic performance.[21,22]

In this study, we hydrothermally synthesized highly biocompatible LC-CDs from *L. chuanxiong*, comprehensively characterized their physicochemical properties, and evaluated their biocompatibility. Through both in vitro cellular models and in vivo AKI rodent models. We hypothesize that LC-CDs could serve as a targeted delivery platform capable of mitochondrial localization and modulation of autophagy-related proteins, thereby exerting synergistic antioxidant, ROS-scavenging, and anti-inflammatory effects. This approach may offer a novel paradigm for AKI treatment by merging the therapeutic merits of herbal medicine with the precision of modern nanotechnology.

Materials and Reagents

Reagents

A 2′,7′-dichlorodihydrofluorescein diacetate (DCFH-DA) assay kit was obtained from Abbkine (China; KTB1910), and a malondialdehyde assay kit was obtained from Tongren Chemical (China; Cat# M496). A bicinchoninic acid (BCA) protein assay kit (P0009) and TUNEL apoptosis detection kits (C1082, C1086) were purchased from Beyotime Biotechnology (China). A JC-1 mitochondrial membrane potential assay kit (MB8650) was obtained from Solarbio (China). Assay kits for creatinine (CRE; Cat# C011-2-1) and blood urea nitrogen (BUN; Cat# C013-2-1) were acquired from Nanjing Jiancheng Bioengineering Institute (China). MitoTrackerRed CMXRos (C1032) was obtained from Beyotime Biotechnology (China). Antibodies were obtained from Cell Signaling Technology (USA), including LC3A/B (12741T), cleaved caspase-3 (14220T), and p62/SQSTM1 (5114T). Anti-β-actin (GB15003-100) was purchased from Servicebio (Wuhan, China), and anti-CD86 (AWA12696) and anti-CD206 (AWA11319) antibodies were purchased from Abiowell (China). Enzyme-linked immunosorbent assay (ELISA) kits for interleukin-6 (IL-6; ER0042), interleukin-1β (IL-1β, ER1094), and tumor necrosis factor-alpha (TNF-α; ER1393) were obtained from FineTest (Wuhan, China). SWE fast-HR electrophoresis buffer (G2081), ice-free rapid transfer buffer (G2028), and electron microscopy fixative solution (G1102) were obtained from Servicebio (China).Catalase (CAT) assay kit (S0051) and total superoxide dismutase (SOD) assay kit (S0101) were obtained from Beyotime (China).

Preparation of LC-CDs

LC-CDs were synthesized through a one-step hydrothermal procedure. The plant material was first finely ground and passed through an 80-mesh sieve, yielding a fine powder. A 50-mL beaker was filled with 0.45 g of this powder and

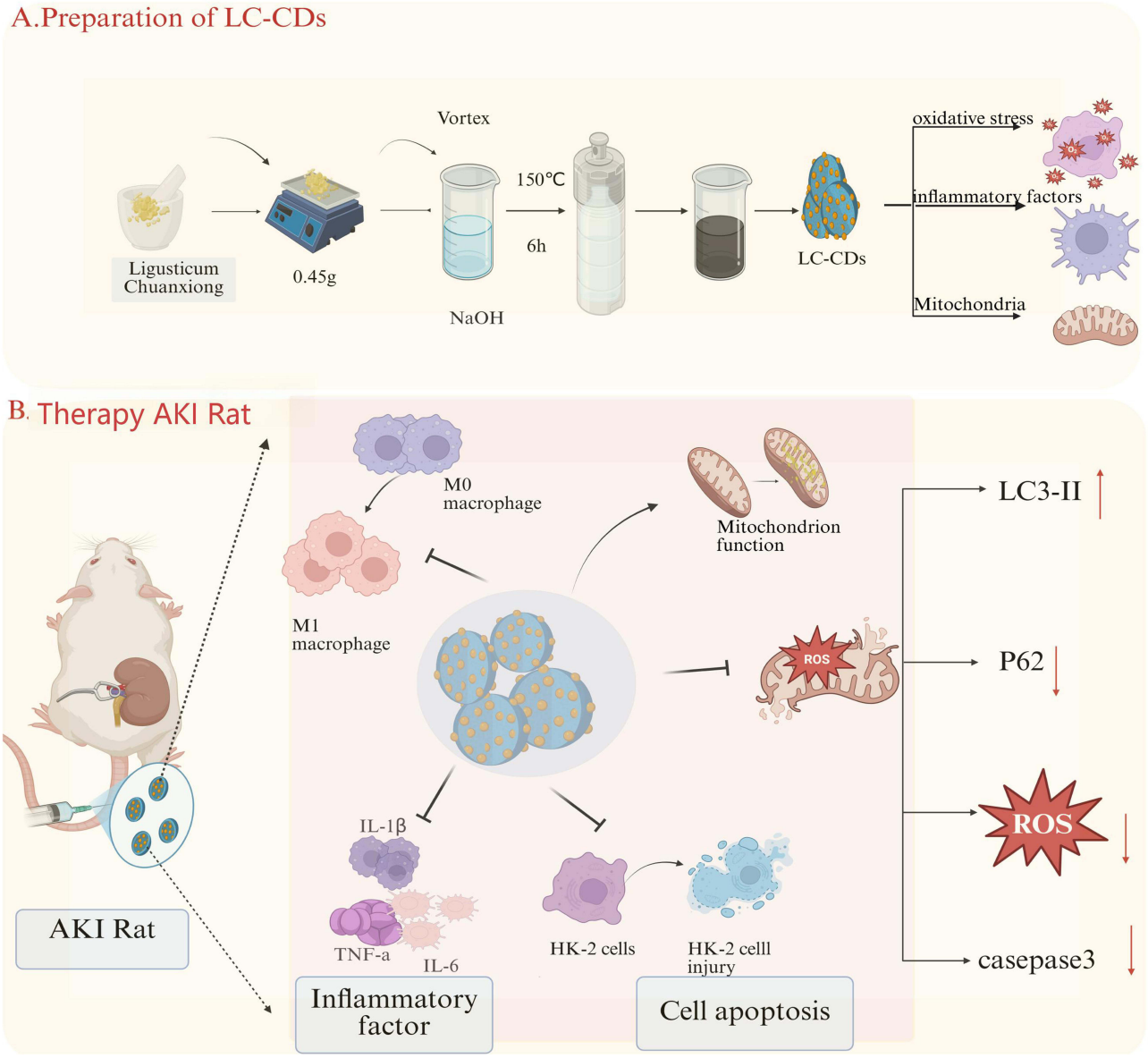

Figure 1 Schematic Overview of Experiment. (**A**) Hydrothermally prepared LC-CDs. (**B**) LC-CDs effectively reduced oxidative stress, which in turn mitigated mitophagy, inhibited apoptosis, and mitigated inflammation. Collectively, these effects restored mitochondrial function, ultimately improving overall AKI outcomes. (**A**) Black arrows indicate preparation process and direction of action. (**B**) Solid black arrows indicate direction of causal relationships. Dashed black arrows indicate biological processes. Solid red arrows indicate key intervention mechanisms.

30 mL of 0.1 mol·L^{-1} NaOH solution. The resulting mixture was subjected to ultrasonic agitation for 10 min and then transferred to a 50-mL Teflon-lined autoclave for hydrothermal processing at 150°C for 6 h. As it cooled to room temperature, the reaction mixture changed from colorless to dark brown, indicating successful synthesis of LC-CDs. Subsequently, the solution was centrifuged at 13,000 rpm for 10 min to remove insoluble residues. The CD-containing supernatant was collected for further use.

Animals and Cell Lines

Specific pathogen-free Sprague Dawley rats weighing 200 to 240 g were obtained from Jinzhou Medical University. All animal procedures were approved by the Research Ethics Committee of Jinzhou Medical University (250165–5) and were conducted in accordance with relevant guidelines established by the People's Republic of China (GB-14925-2010). HK-2 cells were purchased from the American Type Culture Collection (Rockville, MD, USA).

https://doi.org/10.2147/IJN.S577611

AKI Rat Model Construction

Following a 3-day acclimatization period, Sprague Dawley rats were subjected to 15 h of water deprivation, during which they were given unrestricted access to food. AKI was induced through renal I/R. Under anesthesia, the left renal pedicle was clamped for 45 min to induce ischemia. Restoration of the kidney's bright red coloration following clamp removal confirmed reperfusion. The incision was subsequently sutured, and the rats were allowed free access to water and food during recovery.

Animal Grouping and Management

The rats were randomly assigned to one of three groups (n = 6 per group): the control group, which comprised healthy rats receiving intravenous (i.v). injection of phosphate-buffered saline (PBS) through the tail vein; the AKI group, which comprised rats with I/R-induced AKI receiving i.v. injection of saline through the tail vein; and the AKI + LC-CDs group, which comprised AKI rats receiving i.v. injection of LC-CDs (4 mg/kg) through the tail vein. Treatments were administered 24 h after model establishment, and samples were collected at 24 h posttreatment for subsequent analysis.

Measurement of Renal Function Indicators in Sprague Dawley Rats

The rats were anesthetized 24 hours after treatment through an intraperitoneal injection of 3% sodium pentobarbital. Subsequently, blood samples were collected through orbital puncture, and the rats received an anesthesia overdose for humane euthanasia. The blood samples were allowed to stand for 30 min and subsequently centrifuged at 3000 rpm for 25 min to separate the serum. Serum CRE and BUN levels were measured in accordance with the instructions of the assay kit manufacturers.

Biocompatibility Assessment

Hematological analyses were conducted on rat whole blood samples with a hematology analyzer. The leukocyte-related parameters assessed included neutrophilic granulocyte count (GRAN), white blood cell count (WBC), and lymphocyte count (LYM). ELISA kits were used to quantify serum levels of TNF-α, IL-6,aspartate aminotransferase (AST), and alanine aminotransferase (ALT), and IL-1β in accordance with manufacturer guidelines. Biochemical parameters, including CRE and BUN, were also measured with commercial assay kits.

H&E Staining

For hematoxylin and eosin (H&E) staining, paraffin blocks of rat kidney tissue were sectioned at a 4-μm thickness. Sections were deparaffinized in xylene (25 min × 5 cycles), hydrated through a graded ethanol series (10 min), and rinsed in ultrapure water (15 min). The tissues were completely covered with hematoxylin stain for 10–15 min and then thoroughly rinsed under running tap water to remove excess dye. Differentiation was performed in 1% acid-alcohol solution for 1 s with a subsequent 2-min water rinse. After, eosin staining was completed for 5 min, and the sections were then dehydrated in absolute ethanol (5 min × 3 cycles) and cleared in xylene (6 min × 3 cycles). The slides were air-dried in a fume hood for 30 min and mounted with neutral balsam. Light microscopy was performed to photograph and examine the stained sections.

Molecular Docking

The chemical configurations of the compounds were acquired from online databases, and the relevant protein structures were retrieved in Protein Data Bank format from the National Center for Biotechnology Information database. Molecular docking analyses were performed, and structural visualization of the compound–protein interactions was conducted with PyMol software.

Regarding the docking software, all docking experiments were performed with AutoDock Vina 1.2.5, a software widely used because it balances prediction accuracy and computational efficiency in binding mode prediction.

Regarding binding pocket definition, the GetBox plugin in PyMOL was used to precisely define docking pockets. We provided the center coordinates and dimensions (Å) of the binding pocket for each protein−ligand complex to ensure that the docking search space covered known or predicted key binding sites. For the LC3 protein (UniProt ID: Q9GZQ8), the

pocket center and dimensions were (−30.2, 6.0, and 5.3) and (42.6, 50.1, and 42.4) Å, respectively. For the p62/SQSTM1 protein (UniProt ID: Q13501), the pocket center and dimensions were (27.3, 87.7, and 80.5) and (36.8, 45.5, and 48.7) Å, respectively.

In terms of sampling and precision, to ensure sufficient sampling of docking conformations, we changed the key Vina parameter "exhaustiveness" (sampling precision) to 128 from a default value of 8, increasing the depth of conformational search to better identify the global optimal binding mode.

Dihydroethidium Tissue Staining

Rat kidney tissues were harvested and fixed in 4% paraformaldehyde at 4°C for 24 h. Following fixation, the tissues were dehydrated through a graded ethanol series and embedded in paraffin wax. The paraffin-embedded samples were sliced into 5-μm-thick sections with a microtome and mounted onto adhesive-coated glass slides. For deparaffinization and rehydration, the tissue sections were immersed in xylene for 10 min and then washed twice with 100% ethanol for 5 min each. Rehydration was performed through sequential immersion in 95%, 80%, and 70% ethanol and then in distilled water. For dihydroethidium (DHE) staining, we prepared a 5-μM working solution of DHE in PBS. The tissue sections were incubated in this solution for 30 min at 37°C in a dark, humidified chamber to allow DHE to permeate the cells and react with superoxide radicals. After incubation, the sections were washed thrice with PBS, with each wash lasting 5 min, to remove unbound DHE.

TUNEL Staining

Kidney tissues were collected from the experimental animals and immediately fixed in 4% paraformaldehyde at 4°C for 24 h. The fixed tissues were then dehydrated through a graded ethanol series (70%, 80%, 90%, and 100%) for 15−30 min at each step. The tissues were subsequently embedded in paraffin wax to form blocks. Tissue sections (4−5-μm thick) were prepared with a microtome and mounted onto positively charged glass slides. To promote tissue adherence, the slides were baked at 60°C for 1 h. For deparaffinization and rehydration, the sections were immersed in xylene twice for 10 min each time and then washed twice in 100% ethanol for 5 min each time. Rehydration was performed through an ethanol series (95%, 80%, and 70%) followed by a rinse in distilled water. To increase membrane permeability, a working solution of proteinase K (20 μg/mL) was applied to the sections, which were incubated at 37°C for 15–30 min. The sections were then rinsed thrice with PBS for 5 min each wash. They were then immersed in a TUNEL reaction mixture prepared according to the manufacturer's instructions and incubated at 37°C for 1 h in the dark. Following incubation, the sections were rinsed thrice with PBS for 5 min each wash to remove unbound reagents.

Immunohistochemical Staining

Renal tissues were fixed, dehydrated, embedded in paraffin, and sectioned at a thickness of 4 μm. The tissue sections were deparaffinized and rehydrated through sequential immersion in the following solutions: xylene (two washes, 15 min each), absolute ethanol (10 min), 95% ethanol (5 min), 80% ethanol (5 min), 70% ethanol (5 min), ultrapure water (1 min), and PBS with Tween 20 (PBST; three washes, 2 min each). For antigen retrieval, the sections were incubated in preheated 1× Tris-EDTA buffer in a 95°C water bath for 20 min and then allowed to cool for 15 min at room temperature. The sections were then washed three times with PBST (3 min/wash). To quench endogenous peroxidase activity, the sections were incubated in a hydrogen peroxide blocking solution (sufficient to fully cover the tissue) at 37°C for 20 min in a humidified chamber. Subsequently, the sections were washed three times with PBST (3 min/wash). To reduce nonspecific binding, the sections were incubated with 5% BSA at room temperature for 30 min. Primary antibodies [1;2000] were applied, and the sections were incubated overnight at 4°C. After the sections were washed with PBST, horseradish peroxidase−conjugated secondary antibodies [1:100000] were applied and incubated for 1 h at 37°C. Signal development was achieved using DAB substrate applied for 5 min to ensure signal development, after which the sections were counterstained with hematoxylin for 30s and differentiated in 1% acid alcohol. Finally, the sections were dehydrated in a graded ethanol series (70% → 80% → 95% → absolute ethanol), cleared in xylene, and mounted with a resinous medium for microscopic examination.

RNA Sequencing

Total RNA was used as the starting material for RNA library preparation. Magnetic beads conjugated with poly-T oligonucleotides were applied to isolate mRNA from total RNA. Exposure to divalent cations in a heated environment within the first strand synthesis reaction buffer (5×) facilitated mRNA fragmentation, and cDNA for the first strand was generated with a random hexamer primer and M-MuLV reverse transcriptase (RNase H-). Subsequently, the second strand was synthesized with DNA polymerase I in the presence of RNase H. Any remaining overhangs were transformed into blunt ends through exonuclease and polymerase activities. After adenylation of the 3′ ends of the DNA fragments, adaptors with a hairpin loop structure were ligated to enable hybridization. To isolate any cDNA fragments that predominantly measured 370−420 bp, the library fragments were purified with an AMPure XP system. Polymerase chain reaction (PCR) amplification was conducted with Phusion High-Fidelity DNA polymerase, universal PCR primers, and an index (X) primer. The amplified products were then purified again with the AMPure XP system, and an Agilent Bioanalyzer 2100 system was used to evaluate library quality.

Conditioned Medium Model

HK-2 cells were cultured in Dulbecco's modified Eagle medium/F-12 medium supplemented with 10% fetal bovine serum in a humidified incubator under 5% CO_2. Subsequently, the cells were subjected to hypoxic stimulation and treated with LC-CDs.

Annexin V/PI Flow Cytometry

HK-2 cells were seeded into 6-well plates and categorized into normal, hypoxia/reoxygenation (H/R), and LC-CD treatment groups. After the experimental treatments were performed, calcein AM and propidium iodide (PI) stock solutions were equilibrated to room temperature. To prepare the working solution, 30 μL of 1.5 mM PI were mixed with 5 μL of 4 mM calcein AM in 10 mL of PBS. The cells were washed 2–3 times with 1× PBS to remove residual esterase activity. The calcein-AM/PI solution was introduced to the wells, and the plates were incubated at room temperature for 15–20 min in the dark. Cell viability was assessed through fluorescence microscopy: live cells exhibited green fluorescence (calcein AM: Ex/Em = 494/517 nm), whereas dead cells exhibited red fluorescence (PI: Ex/Em = 535/617 nm).

ROS Fluorescence Staining of HK-2 Cells

HK-2 cells were seeded 1 day before experimental treatment to achieve a confluence level of 50–70% at the time of analysis. A test compound was then added at the appropriate concentration to stimulate ROS generation according to experimental requirements. Subsequently, the cells were incubated with the probe (DCFH-DA diluted to a working concentration of approximately 10 μM) in serum-free medium for 30 min in the dark to allow for intracellular uptake. After incubation, the cells were washed 1–2 times with serum-free medium to remove excess, uninternalized DCFH-DA. The fluorescence intensity of the oxidized product, DCF, was measured with a fluorescence microscope, flow cytometer, or plate reader to quantify intracellular ROS levels. For fluorescence detection, the cells were seeded in 6-well, 12-well, or 24-well plates at a density of 5×10^5 cells/well. The excitation and emission wavelengths were set at 488 and 525 nm, respectively.

Detection of Mitochondrial Membrane Potential of HK-2 Cells

To prepare JC-1 working solution, the 200× stock solution was diluted at a ratio of 50 μL to 8 mL in ultrapure water and vortexed until full dissolution. HK-2 cells were digested with trypsin and collected through centrifugation at 300 g for 5 min. The cell pellet was washed twice with 1× PBS, and 10 μL of JC-1 (100×) was added to each well containing culture medium for staining. The cells were thoroughly mixed and incubated at 37°C in a 5% CO_2 incubator for 15–30 min. After incubation, the supernatant was discarded, and the cells were washed twice with 1× PBS. Finally, 500 μL of 1× PBS was added to the cells at room temperature, and the cells were examined under a fluorescence microscope.

Western Blot Analysis

Protein was extracted from the tissue samples with radioimmunoprecipitation assay lysis buffer, as described in the experimental procedures. A BCA assay was performed to quantify protein concentrations. Appropriate separating gels and a 5% stacking gel were prepared according to the molecular weights of the target proteins. Each 10-μg protein sample was loaded into gel wells, and electrophoresis was conducted at a constant voltage of 120 V for 50 min. Following electrophoresis, the proteins were wet-transferred from the gel to polyvinylidene fluoride membranes at a constant current of 400 mA. The membranes were subsequently placed inside an incubation container and blocked with 1× rapid protein blocking solution on a shaker for 15 min. Following blocking, the membranes were washed thrice, with each wash lasting 10 min, with tris-buffered saline with tween-20 (TBST). The excess liquid was carefully removed, and the membranes were incubated overnight at 4°C in a primary antibody solution. Subsequently, the membranes were washed three more times with TBST, with each wash lasting 10 min, and transferred to an incubation container. The membranes were then incubated with the appropriate rabbit or mouse secondary antibody for 60 min at room temperature. Postincubation, the membranes were washed three additional times with TBST, placed in a developing tray, and evenly coated with a 1:1 mixture of chemiluminescent substrates (Solutions A and B). An imaging system was used to visualize protein bands, and grayscale intensity was quantified with Image Lab software.

CAT Activity Assay

We mixed 10 μL of sample with 50 μL of H_2O_2 substrate (65 mM), and this mixture was incubated at 37°C for 2 min. Subsequently, 100 μL of ammonium molybdate solution was added to terminate the reaction. The absorbance was measured at 405 nm. One unit of CAT was defined as the amount of enzyme that decomposed 1 μmol of H_2O_2 per minute at 37°C.

SOD Activity Assay

We mixed 20 μL of sample or blank control with 160 μL of WST-8 working solution and 20 μL of enzyme working solution in 96-well plates. After incubation at 37°C for 20 min, absorbance was measured at 450 nm with a microplate reader. One unit of SOD was defined as the amount of enzyme that inhibited WST-8 reduction by 50%.

Subcellular Fractionation and Localization

Cells were collected through trypsin digestion and centrifugation, and the supernatant was discarded. The cell pellet was washed 1–2 times with precooled PBS. Approximately 1×10^7 cells were resuspended in 1 mL of hypotonic sucrose buffer (0.25 M sucrose, pH 7.4) and homogenized on ice with a homogenizer. The homogenization time was carefully controlled to avoid nuclear rupture, and all procedures were performed with ice-cold reagents at 4°C.

The homogenate was transferred to a centrifuge tube and centrifuged at 600 or 1000 × g for 5–10 min at 4°C. The supernatant, which contained the cytoplasmic fraction (including mitochondria, endoplasmic reticulum, and plasma membrane), was collected for further processing. The pellet, which contained the nuclei (nuclear envelope), was washed with hypotonic sucrose buffer and recentrifuged to remove residual cytoplasmic proteins.

The purified nuclear pellet was resuspended in hypertonic sucrose buffer (1.8 M sucrose, pH 7.4) containing 0.1% NP-40 and homogenized. The sample was then centrifuged at 12,000–20,000 × g for 15–30 min at 4°C. The supernatant contained the nucleoplasm (including ribosomes and chromatin), and the pellet contained the nuclear envelope. To further purify the nuclear envelope, the pellet was subjected to sucrose density gradient centrifugation (0.6/1.2/2.0 M sucrose), and the specific nuclear membrane band was collected.

The cytoplasmic supernatant obtained from the initial low-speed centrifugation was further centrifuged at 11,000 or 10,000 × g for 10–15 min at 4°C. The resulting pellet contained crude mitochondria (including the outer membrane, inner membrane, and matrix), and the supernatant contained the cytoplasmic matrix, lysosomes, and microsomes (including plasma membrane fragments).

To isolate plasma membrane proteins, the microsome-containing cytoplasmic supernatant was treated with a low concentration of Digitonin (approximately 0.01%) and gently agitated at 4°C. This treatment exploited osmotic differences to disrupt the plasma membrane and release cytoplasmic proteins.

Statistical Analysis

Data are presented as the mean ± standard deviation (SD). Each experiment was independently repeated at least three times. We performed two-tailed independent-samples *t*-tests for comparisons between two groups and one-way analysis of variance followed by a Student–Newman–Keuls post hoc test for comparisons involving multiple groups. A significance level (α) of 0.05 was established, with $p < 0.05$ considered significant. Levene's test was conducted to evaluate the homogeneity of variances. All statistical analyses were performed with GraphPad Prism software. The sample size (n) for each analysis is provided in the figure legends.

Results

Synthesis and Characterization of LC-CDs

We used *L. chuanxiong*, a bioactive traditional Chinese medicine, to hydrothermally synthesize LC-CDs. High-resolution transmission electron microscopy revealed a relatively uniform size distribution of quasispherical particles with diameters under 10 nm and good dispersion (Figure 2A and B). Atomic force microscopy further revealed particle sizes from 1.2–1.6 nm (Figure 2C), indicating a pronounced quantum size effect. The LC-CDs demonstrated a high fluorescence quantum yield and unique optical properties, with this contributing to their colloidal stability. The excitation spectrum peaked at 467 nm, corresponding to the $\pi \rightarrow \pi^*$ transition in the polyaromatic conjugated system (Figure 2D). The emission spectrum exhibited excitation-dependent shifts, with a notable emission peak at 590 nm in the yellow light range, indicating that the LC-CDs emitted yellow light under specific excitation wavelengths. Under excitation at 467 nm, valence band electrons absorbed energy and transitioned to the conduction band, forming electron–hole pairs. Their recombination emitted photons, with smaller particle sizes producing larger band gaps and shorter emission wavelengths. X-ray diffraction analysis revealed a broad diffraction peak at 21° corresponding to the (002) plane, with an interlayer spacing of approximately 2.56 Å (Figure 2E). Raman spectroscopy revealed a D band at 1379 cm^{-1}, indicating structural defects and disorder, and a G band at 1569 cm^{-1}, corresponding to in-plane stretching of sp^2 carbon atoms. This pattern reflects the degree of graphitization and structural orderliness of the carbon material (Figure 2F). Low-angle diffraction peaks were generally associated with smaller crystallite sizes and higher defect densities, confirming the nanocrystalline structure of the LC-CDs.

The carbon atom arrangement was less ordered in the LC-CDs compared with in traditional carbon nanomaterials; suggesting a degree of disorder and defects. Defects and disorder create more active sites for carbon materials, increasing their chemical reactivity, catalytic performance, and surface functionalization ability. Surface defects also provide more chemical bonding sites, facilitating the introduction of numerous functional groups. These qualities support the biocompatibility and interaction capabilities of the LC-CDs. Infrared spectroscopy revealed the presence of diverse functional groups on the LC-CD surface, including hydroxyl, carbonyl, carboxyl, C–O, and aromatic carbon structures (Figure 2G). These groups contributed to the observed hydrophilicity, chemical reactivity, and unique optical properties of the LC-CDs, highlighting their promise for application in biomedicine and materials science.

Elemental mapping through energy-dispersive X-ray spectroscopy confirmed the homogenous distribution of C, N, and O (Figure 2K–N). We then conducted X-ray photoelectron spectroscopy to investigate the surface chemistry and valence distribution of the LC-CDs. Three primary peaks were observed in the full spectrum—C1s (285.1 eV), N1s (400.1 eV), and O1s (532.1 eV)—indicating successful nitrogen and oxygen doping on the LC-CD surface (Figure 2H–J). The presence of these rich chemical functional groups enhanced the antioxidant performance and biocompatibility of the LC-CDs. The N1s spectrum exhibited peaks at 299.6 eV, corresponding to pyridinic nitrogen (pyridinic N), and 400.3 eV, corresponding to amino nitrogen, indicating nitrogen incorporation in pyridine-like and amino structures. Pyridinic N can increase electronic conductivity and chemical stability, and amino N contributes to biocompatibility through potential interactions with biomolecules. In the C1s spectrum, four peaks were observed: C=C (284.2 eV), C–C (284.9 eV), C–O/C–N (285.7 eV),

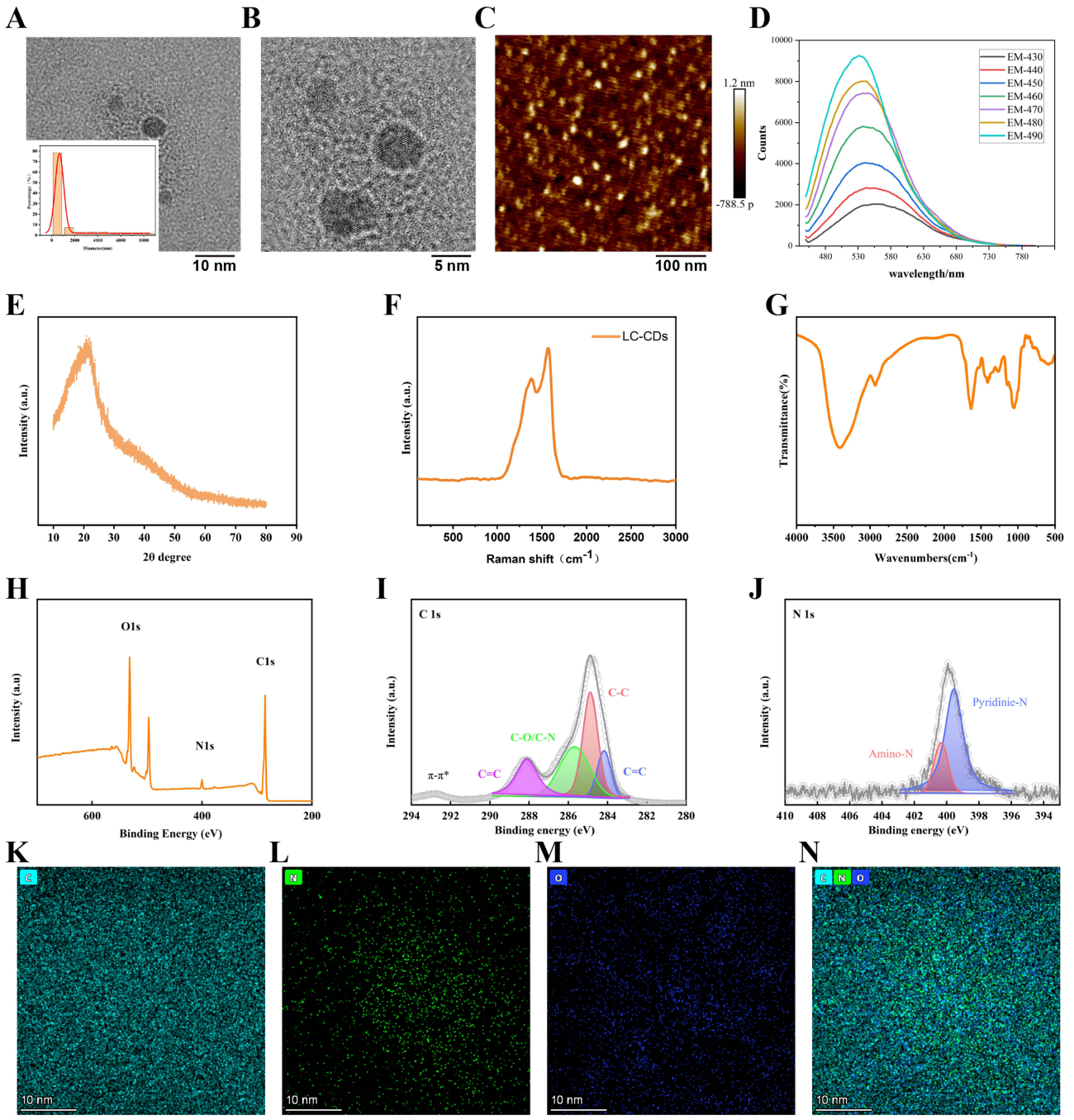

Figure 2 Synthesis and Characterization of LC-CDs. (**A**) Transmission electron microscopy image and particle size distribution histogram of LC-CDs. (**B**) High-resolution transmission electron microscopy image of LC-CD morphology. (**C**) Atomic force microscopy images of LC-CDs (scale bar = 100 nm). (**D**) Emission spectra of LC-CDs under different excitation wavelengths. (**E**) X-ray diffraction spectrum of LC-CDs. (**F**) Raman spectrum of LC-CDs. (**G**) Fourier transform infrared spectrum of LC-CDs. (**H–J**) High-resolution X-ray photoelectron spectra of C1s and N1s for LC-CDs. (**K–N**) Energy-dispersive X-ray spectrum confirming coexistence of C, N, and O (scale bar = 10 nm).

and C=O (288.1 eV; Figure 2F). The C=C and C–C peaks indicated that graphitic and nonconjugated carbon structures, which increase conductivity and chemical stability, were present in the LC-CDs. The C–O/C–N peak indicated the presence of abundant oxygen and nitrogen doping on the LC-CD surface. These doped elements formed functional groups, including hydroxyl, carboxyl, and amino groups, that enhanced the hydrophilicity and biocompatibility of the CDs. The C=O peak further indicated the possible presence of carbonyl or carboxyl groups, which are involved in antioxidant reactions and free-radical scavenging. The oxygen and nitrogen functional groups (ie., hydroxyl, carboxyl, and amino groups) enhanced the

https://doi.org/10.2147/IJN.S577611

hydrophilicity and biocompatibility of the LC-CDs. Nitrogen doping (pyridinic and amino N) and the presence of oxygen-rich groups conferred excellent antioxidant properties and enabled efficient interaction with biomolecules.

In summary, we successfully synthesized LC-CDs with uniform nanostructures, graphitic carbon structures, and the surface presence of multiple chemical functional groups, with these characteristics contributing to the dots' solubility, reactivity, and therapeutic potential. Collectively, these characteristics position LC-CDs as a promising platform for biomedical applications involving targeted antioxidant therapy and drug delivery.

LC-CDs Attenuated Renal Damage in AKI

To evaluate the therapeutic efficacy of the LC-CDs in vivo, an AKI model was induced through unilateral renal I/R. Male Sprague Dawley rats (6–8 weeks old) underwent left renal pedicle clamping for 45 minutes to induce ischemia, followed by reperfusion. The rats received an intravenous injection 24 hours after reperfusion of either saline or LC-CDs (4 mg/kg) through the tail vein. Serum and kidney tissues were collected 24 hours posttreatment for subsequent analysis (Figure 3A).

Histopathological examination of the kidney tissues through H&E staining revealed intact renal architecture in the sham-treated group. Conversely, the I/R-induced AKI group exhibited severe tubular injury characterized by loss of brush borders, tubular dilation, epithelial detachment, and necrosis (Figure 3B). Clinical biomarkers, including significantly elevated serum CRE and BUN levels in the AKI rats (**$p < 0.01$ vs. sham group), confirmed renal dysfunction. Notably, treatment with the LC-CDs markedly reduced serum CRE and BUN levels (**$p < 0.01$ vs. AKI group) (Figure 3C and D). To assess renal targeting, which is critical for successful AKI therapy, ex vivo fluorescence imaging was performed 1, 6, 12, and 24 hours postinjection. The injured kidney exhibited significantly higher fluorescence intensity than the contralateral healthy kidney did, with sustained signal retention up to 24 hours postinjection (Figure 3E), indicating preferential accumulation of LC-CDs in damaged renal tissue. To further validate the cytoprotective effects of the LC-CDs at the cellular level, we established an H/R model using human renal proximal tubular epithelial cells (HK-2). HK-2 cells were exposed to hypoxia (1% O_2, 5% CO_2, and 94% N_2) for 24 hours and then reoxygenated under normoxic conditions (21% O_2 and 5% CO_2) for 24 hours to simulate I/R injury. Cell death was assessed through calcein-AM/PI double staining. Whereas the cells in the control group maintained intact morphology and strong green fluorescence (calcein AM), indicating high viability, the H/R group exhibited a significantly reduced cell count and intense red fluorescence (PI), suggesting extensive cell death. Pretreatment with LC-CDs markedly reduced red fluorescence, confirming improved cell survival and suggesting that LC-CDs effectively inhibit H/R-induced cell death (Figure 3F and G). Collectively, these results demonstrate that LC-CDs not only hold potential to alleviate renal injury, promote functional recovery, and achieve renal targeting in vivo but also exert direct cytoprotective effects at the cellular level.

LC-CDs Mitigated AKI by Reducing Oxidative Stress and Boosting Antioxidant Capacity

To elucidate the therapeutic mechanisms of LC-CDs in AKI, we systematically investigated their ability to alleviate oxidative stress at the cellular and tissue levels. First, we assessed colocalization of LC-CDs with mitochondria in HK-2 cells by using Mito-Tracker Red for mitochondrial labeling. Confocal laser scanning microscopy revealed distinct fluorescence from the mitochondria (red) and LC-CDs (green), with considerable overlap observed between the two signals. Fluorescence colocalization analysis yielded a high Pearson's correlation coefficient of 0.793 (Figure 4A and B). This finding indicates strong mitochondrial localization of the LC-CDs, which may boost ROS scavenging and antioxidant activity. Using a DCFH probe, we monitored intracellular ROS levels. Under H/R conditions, the HK-2 cells exhibited elevated oxidative stress, as indicated by intense green DCF fluorescence. Treatment with the LC-CDs significantly attenuated this fluorescence signal (Figure 4C and D), indicating effective ROS clearance.

To further evaluate the protective effects of the LC-CDs on the cellular antioxidant defense system, we measured SOD and CAT enzyme activity. As illustrated in Figure 4H and I, H/R injury reduced SOD and CAT activity in the HK-2 cells, impairing their ability to scavenge superoxide anions. Treatment with the LC-CDs restored SOD activity. Additionally, H/R injury reduced CAT activity, which is essential for decomposing the hydrogen peroxide generated by SOD. Treatment with the LC-CDs effectively restored CAT activity. At the tissue level, renal oxidative stress was

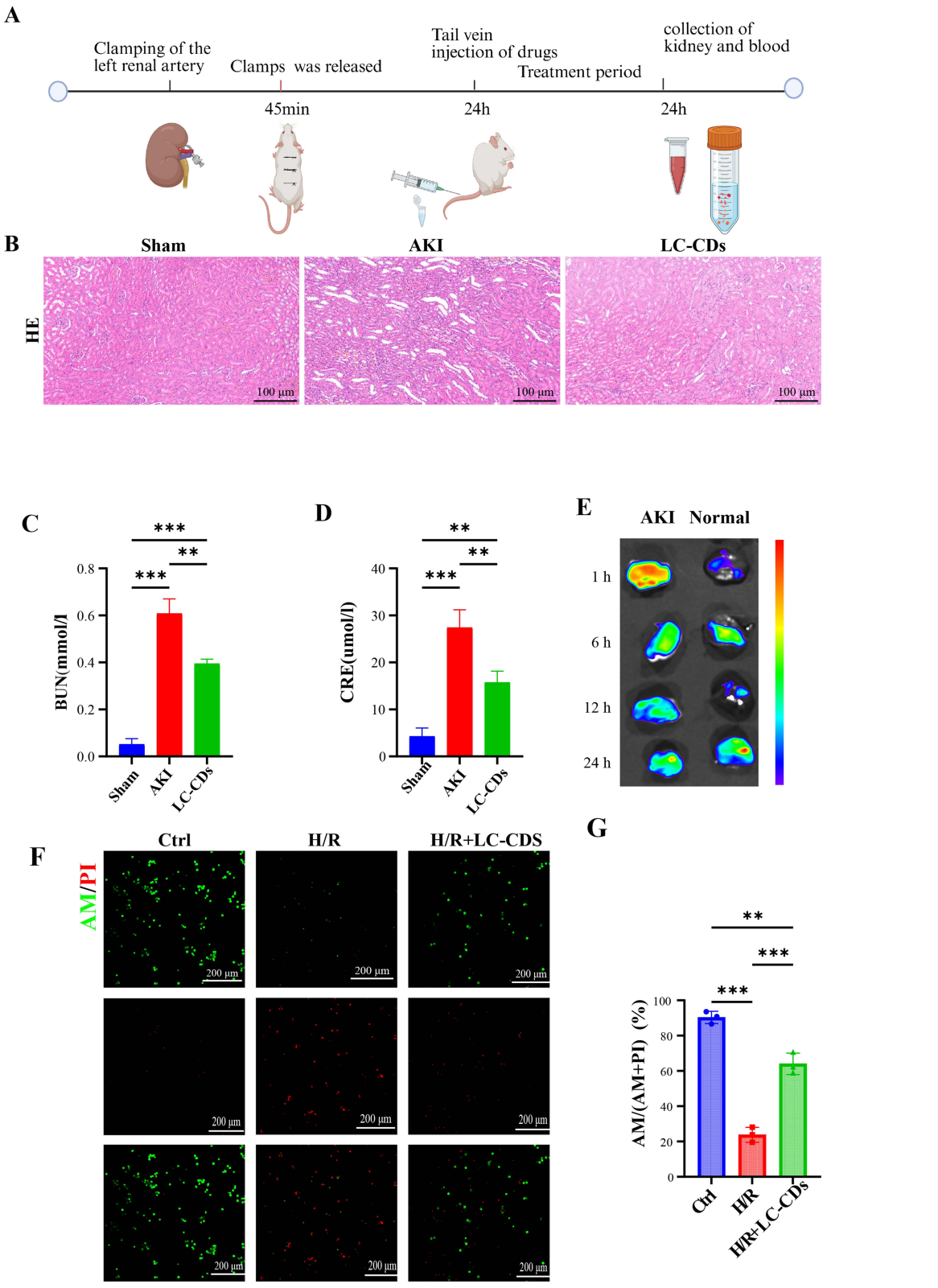

Figure 3 LC-CDs Attenuated Renal Damage in AKI. (**A**) Schematic of AKI model establishment and treatment protocol. (**B**) Representative H&E staining of renal tissues in each treatment group (scale bar = 100 μm). (**C**) Quantification of BUN levels. (**D**) Quantification of CRE levels. (**E**) Time-dependent renal biodistribution of LC-CDs following intravenous injection (1, 6, 12, and 24 h). (**F**) Calcein-AM/PI staining of H/R-stimulated HK-2 cells after 24-hour LC-CD treatment. Green and red fluorescence indicate viable and dead cells, respectively (scale bar = 200 μm). (**G**) Quantitative analysis of live/dead cell ratio. Data are presented as means ± standard deviations. One-way analysis of variance was performed with a post hoc Student–Newman–Keuls test. n = 3, $^{**}p < 0.01$, $^{***}p < 0.001$.

https://doi.org/10.2147/IJN.S577611

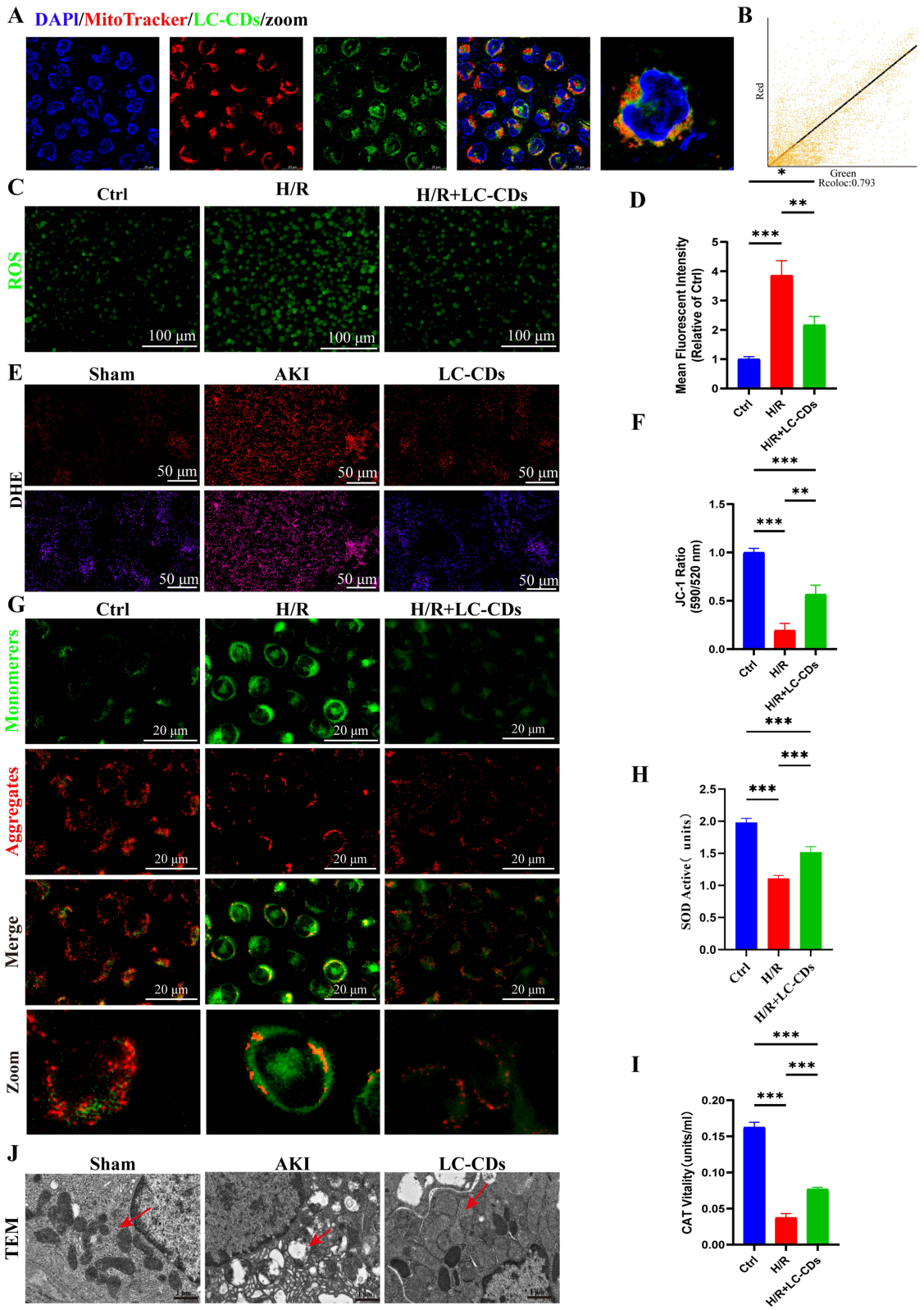

Figure 4 LC-CDs Mitigated AKI Through Mitochondrial Acumulation, Oxidative Stress Reduction, and Antioxidant Effects. (**A**) Confocal microscopy images indicating colocalization of LC-CDs (green) with mitochondria (red) and nuclei (blue) in HK-2 cells (scale bar = 50 μm). (**B**) Colocalization analysis of LC-CDs and mitochondria; Rcoloc = 0.793. (**C**) Representative DCFH-DA fluorescence images of HK-2 cells in each treatment group (scale bar = 100 μm). (**D**) Semiquantitative analysis of ROS fluorescence intensity in HK-2 cells. (**E**) DHE fluorescence images of renal tissues in each treatment group (scale bar = 50 μm). (**F**) Quantification of MMP in each treatment group, presented as the red/green fluorescence intensity ratio (scale bar = 20 μm). (**G**) JC-1 staining for MMP. Red fluorescence indicates JC-1 aggregates; green fluorescence indicates JC-1 monomers (scale bar = 20 μm). (**H**) SOD activity in each group. (**I**) CAT activity in each group. (**J**) Transmission electron microscopy images of mitophagy in each rat treatment group (scale bar = 1 μm; red arrow represents the mitochondria). Data are presented as means ± standard deviations. *$p < 0.05$, **$p < 0.01$, ***$p < 0.001$.

https://doi.org/10.2147/IJN.S577611

assessed through DHE staining. ROS levels were significantly higher in the kidney tissues of AKI rats compared with those in the sham group. ROS levels were substantially reduced after treatment with the LC-CDs (Figure 4E), indicating effective alleviation of renal oxidative stress. JC-1 fluorescence dye was used to evaluate mitochondrial membrane potential (MMP). In H/R-injured cells, JC-1 predominantly existed in monomeric form (green fluorescence), indicating MMP dissipation. Treatment with the LC-CDs promoted MMP recovery, as indicated by increased formation of JC-1 aggregates (red fluorescence; Figure 4F and G). Transmission electron microscopy was employed to examine mitochondrial ultrastructure. Compared with the intact mitochondria observed in the normal group, the mitochondria from the AKI rats exhibited severe matrix dilution, swelling, vacuolization, and cristae disruption. Treatment with the LC-CDs restored mitochondrial morphology and reduced the number of damaged mitochondria (Figure 4J).

RNA Sequencing Revealed Mechanistic Insights Into LC-CDs in AKI

To elucidate the molecular mechanisms underlying AKI and the therapeutic effects of LC-CDs, we performed RNA sequencing on renal tissues from the control, AKI, and LC-CD treatment groups. Correlation analysis was then performed to validate the data's quality and reliability. Principal component analysis heatmaps revealed complete separation of the three groups, indicating distinct transcriptomic profiles and strong correlations within each group (Figure 5A). We then created a Venn diagram illustrating the distribution of differentially expressed genes (DEGs) shared between the AKI and the other two groups (Figure 5B). In the LC-CD treatment group, 4499 genes were upregulated and 3071 were downregulated relative to the AKI group (Figure 5C). We conducted gene ontology enrichment analysis, focusing on biological processes, and observed that these DEGs were significantly associated with immune responses, apoptosis, cell death, and cell differentiation (Figure 5E). These findings suggest that LC-CDs exert therapeutic effects primarily by modulating immune- and apoptosis-related pathways. Kyoto Encyclopedia of Genes and Genomes pathway enrichment further revealed critical signaling pathways affected by LC-CDs, including those related to oxidative phosphorylation, citrate cycle, TNF signaling, apoptosis, cell cycle, and mitophagy (Figure 5D). Gene set enrichment analysis corroborated these results, revealing significant regulation of apoptosis-related pathways following treatment with the LC-CDs (Figure 5F). A hierarchical clustering heatmap of DEG expression profiles revealed distinct gene expression trends between the experimental groups (Figure 5G).

LC-CDs Preserved Mitochondrial Homeostasis By Suppressing Mitophagy and Apoptosis

TUNEL staining revealed significantly more apoptotic cells in the renal tissues of the AKI model rats compared with those of the Sham rats. Treatment with LC-CDs markedly attenuated AKI-induced apoptosis (Figure 6A). Western blot results further confirmed that the LC-CDs suppressed apoptosis by downregulating the essential protein caspase-3 (Figure 6C and F). LC3, a marker protein involved in autophagosome formation, exists in two isoforms: cytosolic LC3-I and membrane-bound LC3-II. LC3-II is a specific marker for mitophagy; its protein concentration is positively correlated with the extent of mitophagy. The p62 protein, another marker of mitophagy, is negatively correlated with mitophagy levels. To compare LC3IIand p62 expression between the three groups of this study, we conducted confocal immunofluorescence imaging. The findings revealed that LC3 levels were significantly lower in the LC-CDs group than in the AKI group, whereas p62 levels were higher in the LC-CDs group than in the AKI group (Figure 6B, I and J). Western blot analysis corroborated these observations (Figure 6D, E, G and H), further confirming that the LC-CDs suppressed mitophagic activity. Subcellular localization analysis (Figure 6K–M) revealed that the LC-CDs exhibited significant colocalization with the autophagy markers LC3-II and p62; signals were predominantly concentrated in mitochondrial regions. Molecular docking analysis (Figure 6N and O) suggested that bioactive components from *L. chuanxiong* may interact with LC3-II and p62 as key autophagic markers, potentially through mechanisms linked to oxidative stress mitigation. Both the computational insights and our experimental observations indicate that LC-CDs may influence mitophagy-related processes by modulating cellular redox balance.

https://doi.org/10.2147/IJN.S577611

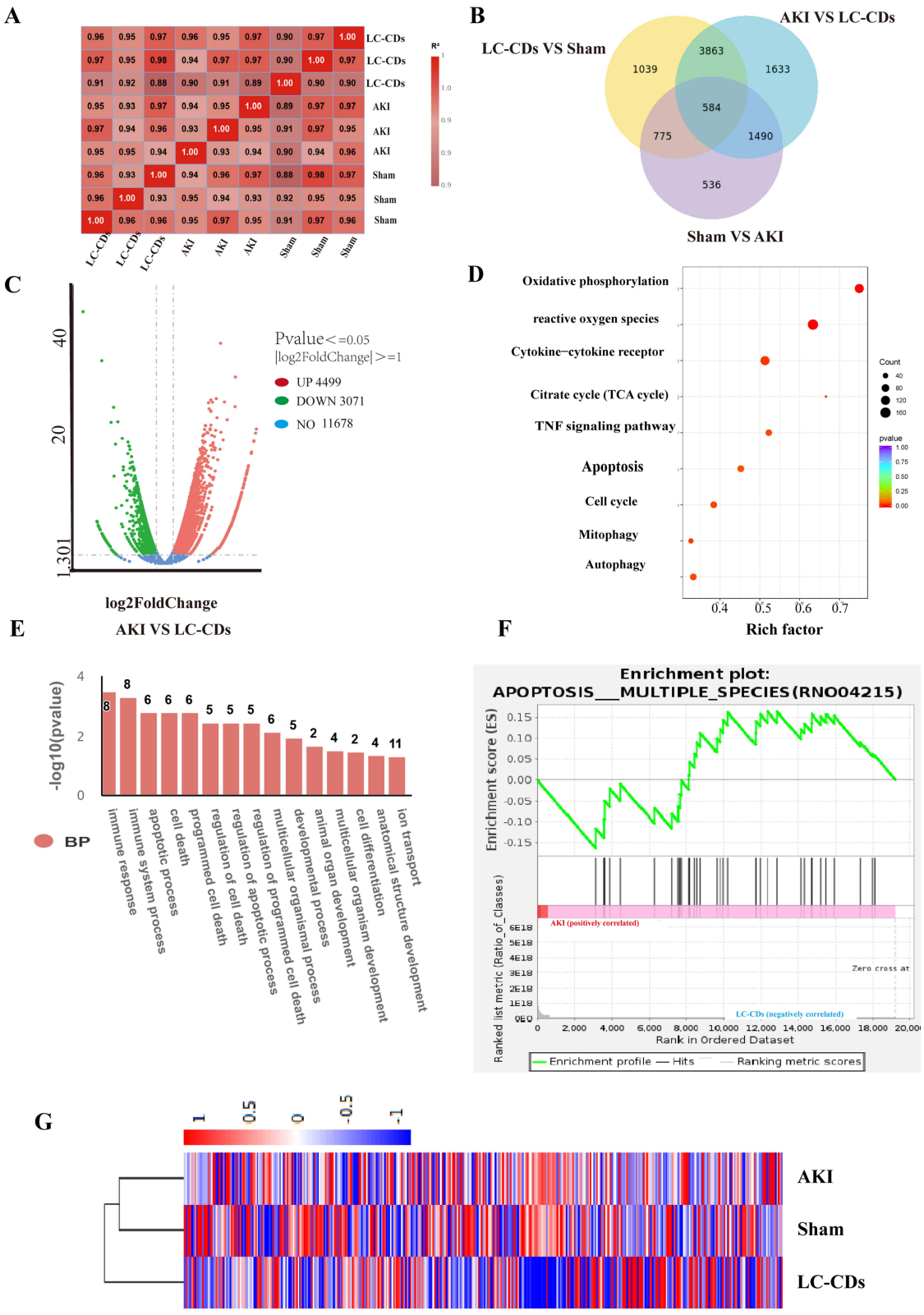

Figure 5 RNA Sequencing of Molecular Mechanisms Driving LC-CD Treatment Effects. (**A**) Correlation heatmap of global gene expression across experimental groups. (**B**) Venn diagram of overlapping DEGs between groups. (**C**) Volcano plot of overlapping DEGs between AKI and LC-CDs groups. (**D**) Kyoto Encyclopedia of Genes and Genomes pathway analysis of overlapping DEGs between AKI and LC-CDs groups. (**E**) Bar chart of significantly enriched gene ontology terms for DEGs. (**F**) Gene set enrichment analysis plot highlighting activation of apoptosis pathways. (**G**) Hierarchical clustering heatmap of DEG expression profiles.

https://doi.org/10.2147/IJN.S577611

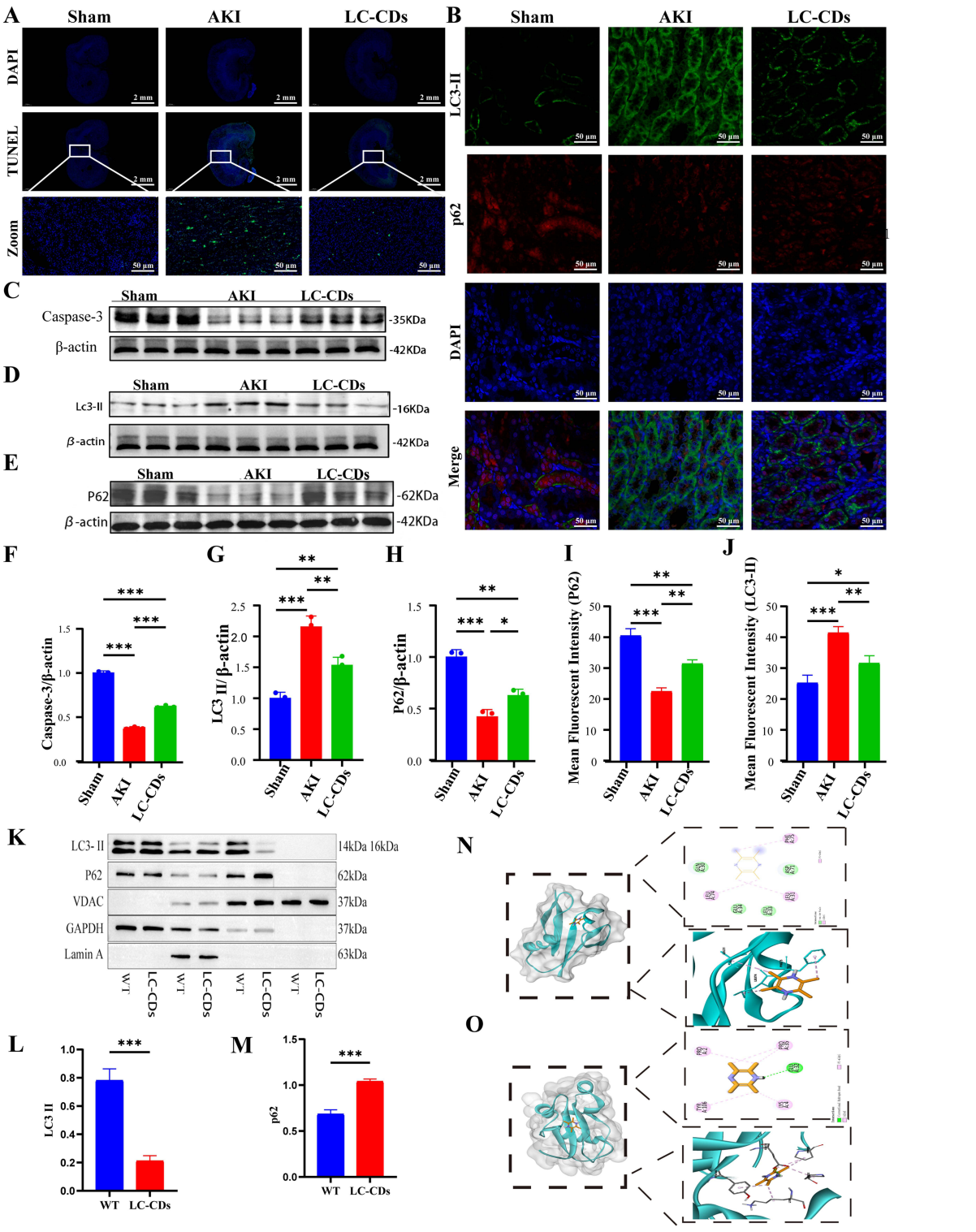

Figure 6 LC-CDs Preserved Mitochondrial Homeostasis By Suppressing Mitophagy and Apoptosis. (**A**) TUNEL fluorescence staining of renal tissues revealing apoptotic cells across treatment groups (scale bar = 2 mm). (**B**) Representative immunofluorescence images of mitophagy markers (green, LC3-II; red, p62) in renal tissues across experimental groups (scale bar = 50 μm). (**C**) Western blot analysis of apoptosis-related protein (caspase-3) expression in rat kidney tissues in each treatment group. (**D** and **E**) Western blot analysis of mitophagy-related proteins (LC3-II and p62) in rat kidney tissues in each treatment group. (**F**) Grayscale quantification of caspase-3 expression. (**G** and **H**) Grayscale quantification of p62 and LC3-II expression. (**I** and **J**) Corresponding semiquantitative analysis of fluorescence intensity in HK-2 cells. (**K**–**M**) Representative Western blots of LC3-II, p62, laminA, GAPDH, and VDAC from subfractions of HK-2 cells. Lamin A, GAPDH, and VDAC were used as markers of nuclear, cytosolic, and mitochondrial fractions, respectively. (**N** and **O**) Molecular docking simulations of *L. chuanxiong* components with LC3-II and p62. Dashed box highlights interaction interface between the protein receptor ligand and core binding domain, which is critical for predicting binding affinity and stability. Data are presented as means ± SDs. One-way analysis of variance was performed with a post hoc Student–Newman–Keuls test. n = 3, *$p < 0.05$, **$p < 0.01$, ***$p < 0.001$.

https://doi.org/10.2147/IJN.S577611

LC-CDs Inhibited Macrophage Activation and Alleviated Inflammatory Response

In AKI, NADPH oxidase and mitochondria generate ROS, contributing to oxidative stress, which plays a crucial role in macrophage polarization during inflammation.[20] Macrophages therefore play a major role in AKI progression. We identified CD86 and CD206 as markers of M1 and M2 macrophage phenotypes, respectively. To investigate the anti-inflammatory effects of the developed LC-CDs, we conducted immunofluorescence staining for CD86 and CD206 expression. Figure 7A illustrates the mechanism by which the LC-CDs exerted anti-inflammatory effects. We observed a marked increase in M1 macrophages (CD86) and a reduction in M2 macrophages (CD206) following AKI treatment. By contrast, LC-CD treatment reduced CD86 expression and increased CD206 expression in kidney tissues (Figure 7B). Western blot analysis further corroborated these findings (Figure 7D, H and I). In AKI, macrophage infiltration into damaged kidneys is accompanied by the release of proinflammatory mediators, which exacerbates the inflammatory response. To evaluate the anti-inflammatory effects of LC-CDs in AKI, we conducted immunohistochemical analysis and an ELISA. The immunohistochemistry results revealed significantly elevated IL-6, IL-1β, and TNF-α levels in the AKI group. Treatment with LC-CDs reduced IL-6, IL-1β, and TNF-α levels (Figure 7C). ELISA measurements of serum cytokine levels revealed similar trends (Figure 7E–G), supporting these results. The LC-CDs demonstrated a capacity to effectively prevent M1 macrophage polarization and facilitate the transition to the M2 phenotype, reducing the release of harmful proinflammatory components in the AKI microenvironment. This effect may be related to the effective scavenging of ROS and oxidative stress alleviation demonstrated by the LC-CDs.

Biocompatibility and Safety Evaluation of LC-CDs

We systematically evaluated the in vivo biocompatibility and safety of the LC-CDs synthesized from *L. chuanxiong* in a rat model (Figure 8A and B). LC-CDs (4 mg/kg) were administered through tail vein injection. After 24 h, we prepared and performed H&E staining on pathological sections of key organs, including the heart, liver, spleen, lung, and kidney (Figure 8C). No apparent pathological alterations or tissue damage were observed in the LC-CDs group relative to in the PBS control group. Additionally, we assessed liver function markers (ALT and AST; Figure 8D and E), inflammatory cytokine expression (TNF-α, IL-6, and IL-1β; Figure 8F, G and H), renal function metrics (BUN and CRE; Figure 8L and M), and hematological variables (GRAN, WBC, and LYM; Figure 8I, J and K). No parameter differed significantly between the treatment and control groups, indicating no systemic inflammatory response. These results support the excellent biocompatibility and safety profile of the developed LC-CDs.

Discussion

AKI has a multifactorial pathophysiology that involves a self-perpetuating cycle of oxidative stress, inflammatory activation,[23,24] mitochondrial dysfunction, and programmed cell death.[25,26] Renal I/R injury is a common etiology of AKI, initiating a cascade in which ROS overproduction damages cellular structures,[27,28] triggers mitochondrial permeability transition, and amplifies inflammatory signaling.[29,30]

The complex interplay between oxidative stress and dysregulated inflammation is a central pathogenic driver of AKI, particularly when I/R injury is involved, posing a critical therapeutic challenge.[31,32] Effective biocompatible agents are required that are capable of disrupting this vicious cycle. Addressing this unmet need, we successfully synthesized LC-CDs and demonstrated their therapeutic efficacy in a renal I/R model.

Within the expanding field of plant-derived DCs for renal therapy, our LC-CDs have common therapeutic targets with other proposed agents but offer distinct advantages. As is true for other bioactive CDs, such as mulberry-derived CDs[33] and those that activate adenylate cyclase,[34] our LC-CDs demonstrated potent ROS scavenging and anti-inflammatory efficacy. We further observed their uniquely preferential mitochondrial accumulation and subsequent mitigation of oxidative stress at the organelle level. The targeted action and ultra-small size of the LC-CDs (<2 nm) enables efficient glomerular filtration and renal accumulation, overcoming the limitations of antioxidant therapies that lack specificity.

The therapeutic efficacy of our LC-CDs is rooted in their unique physicochemical properties. Their oxygen-rich surface functional groups and extended sp^2-conjugated domains confer potent multienzyme mimetic activities, resembling SOD, CAT, and peroxidase. These activities enable direct, rapid scavenging of ROS, which prevents oxidative damage to mitochondrial

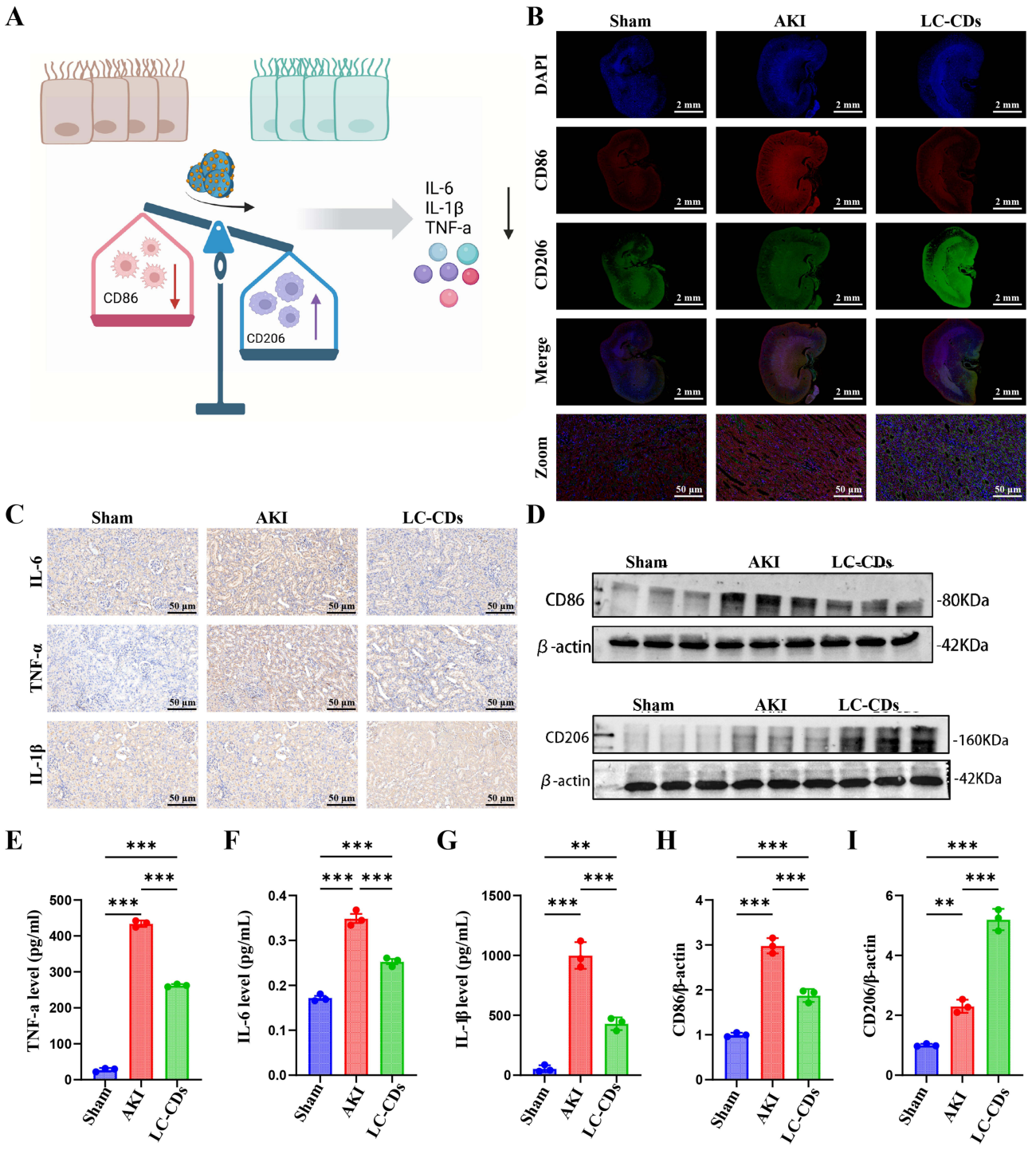

Figure 7 LC-CDs Inhibited Macrophage Activation and Alleviated Inflammatory Responses. (**A**) Schematic of proposed mechanism through which LC-CDs inhibit macrophage activation and reduce proinflammatory cytokine production. (**B**) Representative immunofluorescence images of colocalization of CD86 (red) and CD206 (green) in renal tissues across experimental groups (scale bar = 2 mm). (**C**) Representative immunohistochemical images of IL-6, TNF-α, and IL-1β expression in rat kidney sections across treatment groups (scale bar = 50 μm). (**D**) Western blot analysis of CD86 and CD206 protein levels in renal tissues. (**E**–**G**) Renal tissue levels of inflammatory cytokines (IL-6, TNF-α, and IL-1β) across treatment groups. (**H** and **I**) Quantitative analysis of CD86 and CD206 protein expression. Data are presented as means ± SDs (n = 3). One-way analysis of variance was performed with a post hoc Student–Newman–Keuls test. $^{**}p < 0.01$, $^{***}p < 0.001$.

membranes, inhibits cytochrome c release, and suppresses apoptotic cascade effects, as corroborated by the recovery of MMP observed in our models.

In addition to direct antioxidant effects, our transcriptomic and protein analyses robustly implicated the autophagy pathway in the therapeutic action of the LC-CDs. We observed an accumulation of LC-CDs around mitochondria. Further

https://doi.org/10.2147/IJN.S577611

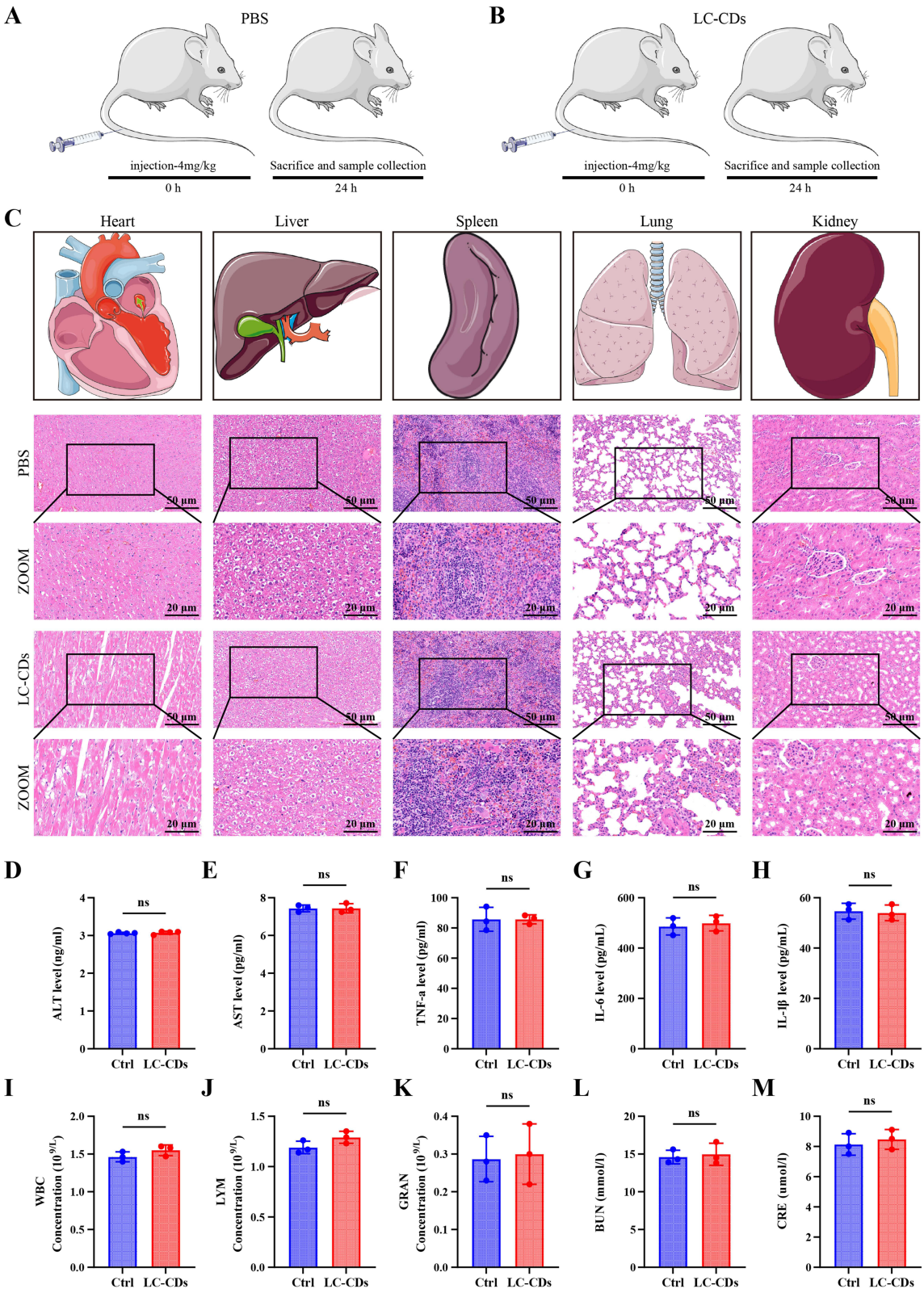

Figure 8 Biocompatibility and Safety Evaluation of LC-CDs. (**A** and **B**) Schematic overview of biosafety evaluation protocol for LC-CDs. (**C**) Representative H&E staining of major organs (heart, liver, spleen, lungs, and kidneys; scale bar = 50 μm, main panels = 20 μm, insets and magnified views). (**D** and **E**) Liver function indicators. (**F**–**H**) Inflammatory cytokine levels. (**I**–**K**) Hematological parameters. (**L** and **M**) Kidney function indicators. Data are presented as means ± SDs; n = 3. ns, nonsignificant ($p > 0.05$).

https://doi.org/10.2147/IJN.S577611

RNA sequencing analysis and biological assays revealed a potential mechanism in which the LC-CDs activate the key autophagy proteins LC3-II and p62, thereby facilitating the clearance of damaged mitochondria, reducing ROS accumulation, alleviating oxidative stress, and mitigating inflammatory responses. To explore a structural basis for this interaction, we performed in silico molecular docking analysis between key herbal precursor motifs (representing LC-CD surface chemistry) and core autophagy proteins (p62 and LC3-II), and we observed a binding affinity. This result serves as a computational hint rather than as definitive proof of direct nanomaterial–protein binding in vivo. Because LC-CDs are complex nanomaterials with interactions governed by collective surface properties, the proposed model is a simplification. Our results should be interpreted as hypothesis generating, and future validation involving surface plasmon resonance with purified LC-CDs or related techniques must be conducted.

Although we focused on investigating the mechanism by which the LC-CDs alleviate oxidative stress during the acute phase through mitochondrial targeting and ROS scavenging rather than on validating their long-term efficacy in chronic fibrosis or the transition from AKI to CKD, our findings provide preliminary theoretical support for LC-CDs as a nanomaterial with both acute renoprotective effects and potential antichronicity functions. The multitarget, multistage therapeutic potential of LC-CDs aligns with recommendations for clinical use of rationally designed nanomedicines to address complex disease progression.

Despite these promising results, this study has several limitations that should be addressed in future research. First, while our findings support the therapeutic efficacy of LC-CDs in a hypoxia-induced AKI model, this study focused on a single etiology—namely, ischemia–reperfusion injury. AKI in clinical settings often arises from diverse causes such as sepsis, which involves not only mitochondrial oxidative stress but also systemic inflammation and hemodynamic alterations that may not be fully recapitulated in the current model. Therefore, validation in larger cohorts and across different AKI etiologies (eg., sepsis-induced models) is necessary to confirm the broader applicability of LC-CDs. Second, the short-term (24-hour) safety profile must be validated in longer-term (eg., 7–14 day) toxicity and biodistribution studies to achieve comprehensive assessment of translational viability. Third, the precise cellular uptake mechanism of the LC-CDs requires further elucidation. Fourth, orthogonal experimental approaches must be employed to rigorously confirm our compelling but preliminary evidence linking LC-CDs to autophagy regulation, including our docking predictions. Fifth, while our RNA sequencing data provided valuable transcriptomic insights, these findings are preliminary and necessitate future validation using orthogonal techniques such as quantitative real-time PCR to confirm gene-level expression changes. Addressing these limitations in future comparative investigations will help delineate the versatility of this nanoplatform and support the development of pathophysiology-specific nanotherapies for acute kidney injury.[35]

Conclusion

In summary, this study successfully synthesized and characterized LC-CDs derived from a natural herbal source. The developed LC-CDs exhibited potent antioxidant activity and free radical scavenging capacity, attributable to their unsaturated functional groups. In a rat model of acute kidney injury (AKI), LC-CDs demonstrated significant therapeutic efficacy, coupled with favorable biocompatibility and safety profiles, underscoring their potential for clinical translation. Mechanistically, these protective effects were mediated by the accumulation of LC-CDs around mitochondria and their interaction with key mitophagy regulators, LC3-II and p62. This engagement facilitated effective reactive oxygen species (ROS) scavenging, preservation of mitochondrial integrity, and suppression of oxidative stress and inflammation. Collectively, these findings provide novel insights into the therapeutic potential of herbal-derived carbon dots in AKI, positioning LC-CDs as a promising nanomaterial with translational relevance for the management of acute kidney injury.

Abbreviations

AKI, acute kidney injury; LC-CDs, *Ligusticum chuanxiong* carbon quantum dots; ROS, reactive oxygen species; I/R, renal ischemia-reperfusion; CAT, catalase, SOD, superoxide dismutase.

Data Sharing Statement

Data available on request from the corresponding author.

Ethical Considerations

All animal experiments in this study were approved by the Animal Care and Use Committee of Jinzhou Medical University (Ethical Approval No. 250165-5). All procedures were performed in accordance with relevant national guidelines and institutional regulations for the ethical treatment of laboratory animals.

Acknowledgments

This work was supported by the Liaoning Provincial Department of Education University Basic Research Project - Local Service Project (LJ212510160017), the Liaoning Provincial Science and Technology Plan Joint Plan Fund (No. 2023JH2/101700233), the Liaoning Medical Education Research Project (Grant No. 2024-N004-06), and the Liaoning Economic and Social Development Research Program (Grant No. 2025lslqnkt-013).

Author Contributions

All authors made significant contributions to the work reported, whether in the conception, study design, execution, acquisition of data, analysis, and interpretation, or in all these areas; took part in drafting, revising, or critically reviewing the article; gave final approval of the version to be published; have agreed on the journal to which the article has been submitted; and agree to be accountable for all aspects of the work.

Disclosure

The authors declare that they have no conflicts of interest.

References

1. Abramov E, Garti N. Incorporation of curcumin in liquid nanodomains embedded into polymeric films for dermal application. *Colloids Surf B Biointerfaces*. 2021;198:111468. doi:10.1016/j.colsurfb.2020.111468
2. Zhou X, Wang N, Zhao B, Liu Z, Yu P. Precision medicine for acute kidney injury: baicalein-nanodrug delivery system combat oxidative stress and repair mitochondrial dysfunction. *Int J Pharm*. 2025;678:125694. doi:10.1016/j.ijpharm.2025.125694
3. Xie W, Gao L, Gu X, et al. Ischemic preconditioning attenuates ischemia/reperfusion-induced acute kidney injury dependent on mitochondrial protease CLPP. *IUBMB Life*. 2025;77(4):e70015. doi:10.1002/iub.70015
4. Su L, Zhang J, Gomez H, Kellum JA, Peng Z. Mitochondria ROS and mitophagy in acute kidney injury. *Autophagy*. 2023;19(2):401–414. doi:10.1080/15548627.2022.2084862
5. Lane SF, Harvey-Jones E, Ward O, Davies R. Renal replacement and extracorporeal therapies in critical care: current and future directions. *Acute Med*. 2023;22(3):154–162.
6. Wang Y, Wu L, Wang H, et al. *Ligusticum chuanxiong*: a chemical, pharmacological and clinical review. *Front Pharmacol*. 2025;16:1523176. doi:10.3389/fphar.2025.1523176
7. Long Y, Yu S, Li D, et al. Preparation, characterization and safety evaluation of *Ligusticum chuanxiong* essential oils liposomes for treatment of cerebral ischemia-reperfusion injury. *Food Chem Toxicol*. 2023;175:113723. doi:10.1016/j.fct.2023.113723
8. Qi XY, Peng GC, Han QT, et al. Phthalides from the rhizome of *Ligusticum chuanxion*g Hort. attenuate diabetic nephropathy in mice. *J Ethnopharmacol*. 2024;319(Pt 2):117247. doi:10.1016/j.jep.2023.117247
9. Chen X, Zhang X, Sun W, et al. LcSAO1, an unconventional DOXB Clade 2OGD enzyme from *Ligusticum chuanxiong* catalyzes the biosynthesis of plant-derived natural medicine butylphthalide. *Int J Mol Sci*. 2023;24(24). doi:10.3390/ijms242417417
10. Zhu FQ, Ma JY, Zhang YY, Yu Y. Research progress on mechanisms and pharmacokinetics of ligustilide in treatment of locomotor system diseases. *Zhongguo Zhong Yao Za Zhi*. 2024;49(24):6625–6634. doi:10.19540/j.cnki.cjcmm.20240716.701
11. He S, Li X, He Y, et al. High-density lipoprotein nanoparticles spontaneously target to damaged renal tubules and alleviate renal fibrosis by remodeling the fibrotic niches. *Nat Commun*. 2025;16(1):1061. doi:10.1038/s41467-025-56223-z
12. Rosenblum D, Gutkin A, Kedmi R, et al. CRISPR-Cas9 genome editing using targeted lipid nanoparticles for cancer therapy. *Sci Adv*. 2020;6(47). doi:10.1126/sciadv.abc9450
13. Yunus U, Zulfiqar MA, Ajmal M, et al. Targeted drug delivery systems: synthesis and in vitro bioactivity and apoptosis studies of gemcitabine-carbon dot conjugates. *Biomed Mater*. 2020;15(6):065004. doi:10.1088/1748-605X/ab95e1
14. Jing HH, Bardakci F, Akgöl S, et al. Green carbon dots: synthesis, characterization, properties and biomedical applications. *J Funct Biomater*. 2023;14(1). doi:10.3390/jfb14010027
15. Zhao Y, Wang S, Wei Z, et al. Natural toolbox-chemical engineering aspect and high-value applications of janus cellulose nanomaterials. *Adv Sci*. 2025;12(28):e00820. doi:10.1002/advs.202500820
16. Guo Q, Lu X, Zhang Y, et al. A nanoplatform targeting cascade pathways for enhanced triptolide delivery in acute kidney injury therapy. *Adv Healthc Mater*. 2025;14(16):e2500595. doi:10.1002/adhm.202500595
17. Qin W, Tian H, Feng X, Tang Z. Iron and copper codoped carbon nanodots as oxidase mimics and fluorescent probes for detection of phenol and dimethoate. *Spectrochim Acta A Mol Biomol Spectrosc*. 2025;331:125794. doi:10.1016/j.saa.2025.125794
18. Zhang B, Wang B, Ushakova EV, et al. Assignment of core and surface states in multicolor-emissive carbon dots. *Small*. 2023;19(31):e2204158. doi:10.1002/smll.202204158

19. Tang T, Zhang J, Wang Y, et al. Precision-Engineered silver single-atom carbon dot nanozymes for theranostic management of acute kidney injury. *Adv Sci*. 2026:e19393. doi:10.1002/advs.202519393
20. Deng H, Qu Y, Chu B, et al. Macrophage membrane-biomimetic ROS-responsive platinum nanozyme clusters for acute kidney injury treatment. *Biomaterials*. 2025;317:123072. doi:10.1016/j.biomaterials.2024.123072
21. Soe H, Loftsson T, Jansook P. The application of cyclodextrins in drug solubilization and stabilization of nanoparticles for drug delivery and biomedical applications. *Int J Pharm*. 2024;666:124787. doi:10.1016/j.ijpharm.2024.124787
22. Sturabotti E, Sierra-Serrano B, Apresto SM, et al. Carbon dots as multi-modal contrast agents: opportunities and open challenges for in vivo bioimaging. *Adv Drug Deliv Rev*. 2025;224:115659. doi:10.1016/j.addr.2025.115659
23. Wu W, Lan W, Jiao X, et al. Pyroptosis in sepsis-associated acute kidney injury: mechanisms and therapeutic perspectives. *Crit Care*. 2025;29 (1):168. doi:10.1186/s13054-025-05329-3
24. Fu H, Wang Y, Huang B, et al. Tannic acid-cerium nanoenzymes serve as broad-spectrum antioxidants to alleviate acute kidney injury by modulating macrophage polarization, mitophagy and endoplasmic reticulum stress. *J Control Release*. 2025;380:892–909. doi:10.1016/j.jconrel.2025.02.038
25. Rius-Pérez S, Pérez S, Toledano MB, Sastre J. Mitochondrial reactive oxygen species and lytic programmed cell death in acute inflammation. *Antioxid Redox Signal*. 2023;39(10–12):708–727. doi:10.1089/ars.2022.0209
26. Liu D, Qin H, Gao Y, Sun M, Wang M. Cardiovascular disease: mitochondrial dynamics and mitophagy crosstalk mechanisms with novel programmed cell death and macrophage polarisation. *Pharmacol Res*. 2024;206:107258. doi:10.1016/j.phrs.2024.107258
27. Huang C, Deng Y, Ma R, et al. A metal-organic cage-derived cascade antioxidant nanozyme to mitigate renal ischemia-reperfusion injury. *Nanoscale*. 2024;16(19):9406–9411. doi:10.1039/d4nr00742e
28. Wang Y, Dillon KM, Li Z, Winckler EW, Matson JB. Alleviating cellular oxidative stress through treatment with superoxide-triggered persulfide prodrugs. *Angew Chem Int Ed Engl*. 2020;59(38):16698–16704. doi:10.1002/anie.202006656
29. Chen M, Liang Z, Sun M, et al. Aryl hydrocarbon receptor-induced activation of AIM2 inflammasome is mediated by MOMP and MPT: a vital therapeutic pathway for inflammation. *Cell Rep*. 2025;44(12):116673. doi:10.1016/j.celrep.2025.116673
30. Xian H, Watari K, Sanchez-Lopez E, et al. Oxidized DNA fragments exit mitochondria via mPTP- and VDAC-dependent channels to activate NLRP3 inflammasome and interferon signaling. *Immunity*. 2022;55(8):1370–1385.e8. doi:10.1016/j.immuni.2022.06.007
31. Zhang J, Luan ZL, Huo XK, et al. Direct targeting of sEH with alisol B alleviated the apoptosis, inflammation, and oxidative stress in cisplatin-induced acute kidney injury. *Int J Biol Sci*. 2023;19(1):294–310. doi:10.7150/ijbs.78097
32. Mard SA, Hoseinynejad K, Nejaddehbashi F. Gallic acid improves therapeutic effects of mesenchymal stem cells derived from adipose tissue in acute renal injury following rhabdomyolysis induced by glycerol. *Inflammation*. 2022;45(6):2294–2308. doi:10.1007/s10753-022-01691-4
33. Lu Z, Li H, Song N, et al. Therapeutic potential of carbon dots derived from phytochemicals as nanozymes exhibiting superoxide dismutase activity for anemia. *ACS Appl Mater Interfaces*. 2025;17(3):4562–4578. doi:10.1021/acsami.4c17885
34. Wei Z, Wang L, Yang L, et al. Chirality-Driven metal-phenolic artificial enzymes enable renal targeting and antioxidative therapy enhancement for acute kidney injury. *J Am Chem Soc*. 2025;147(50):45977–45998. doi:10.1021/jacs.5c12337
35. Wang L, Li ZY, Zhong CL, et al. Therapeutic potential of naturally derived carbon dots in sepsis-associated acute kidney injury. *Chin Med*. 2025;20 (1):49. doi:10.1186/s13020-025-01103-3